Computers and Geotechnics 80 (2016) 360–372

Contents lists available at ScienceDirect

Computers and Geotechnics

journal homepage: www.elsevier.com/locate/compgeo

3D multiscale modeling of strain localization in granular media

Ning Guo *, Jidong Zhao

Department of Civil and Environmental Engineering, The Hong Kong University of Science and Technology, Clear Water Bay, Kowloon, Hong Kong

ARTICLE INFO

Article history:
Available online 9 February 2016

Keywords:
Hierarchical multiscale approach
3D simulation
Strain localization
Diffuse failure
FEM/DEM
Granular media

ABSTRACT

A hierarchical multiscale modeling approach is used to investigate three-dimensional (3D) strain localization in granular media. Central to the multiscale approach is a hierarchical coupling of finite element method (FEM) and discrete element method (DEM), wherein the FEM is employed to treat a boundary value problem of a granular material and the required constitutive relation for FEM is derived directly from the DEM solution of a granular assembly embedded at each of the FEM Gauss integration points as the representative volume element (RVE). While being effective in reproducing the complex mechanical responses of granular media, the hierarchical approach helps to bypass the necessity of phenomenological constitutive models commonly needed by conventional FEM studies and meanwhile offers a viable way to link the macroscopic observations with their underlying microscopic mechanisms. To model the phenomenon of strain localization, key issues pertaining to the selection of proper RVE packings are first discussed. The multiscale approach is then applied to simulate the strain localization problem in a cubical specimen and a cylindrical specimen subjected to either conventional triaxial compression (CTC) or conventional triaxial extension (CTE) loading, which is further compared to a case under plane-strain biaxial compression (PBC) loading condition. Different failure patterns, including localized, bulging and diffuse failure modes, are observed and analyzed. Amongst all testing conditions, the PBC condition is found most favorable for the formation of localized failure. The CTC test on the cubical specimen leads to a 3D octopus-shaped localization zone, whereas the cylindrical specimen under CTC shows seemingly bulging failure from the outlook but rather more complex failure patterns within the specimen. The CTE test on a uniform specimen normally ends in a diffuse failure. Different micro mechanisms and controlling factors underlying the various interesting observations are examined and discussed.

1. Introduction

Loading paths and conditions affect many aspects of the shear behavior of a granular medium, including its peak and residual strength, deformation responses and failure patterns. As shown by Uthayakumar and Vaid [1] and Yoshimine et al. [2], a sand sample sheared under the undrained condition may show a hardening response in conventional triaxial compression (CTC), whereas it may fail in form of static liquefaction in conventional triaxial extension (CTE) at the same initial density. Another prominent example is slope stability analysis. The factor of safety derived for a slope based on 2D plane strain assumption may differ substantially from that based on a full 3D analysis [3]. Instabilities and failures of sand have been widely related to catastrophic hazards such as landslides and debris flow in geotechnical engineering and have hence become a focal topic of research in geomechanics. Compelling experimental evidence indicates that loading conditions may dictate the occurrence of instability patterns in sand, in conjunction with other key factors such as density and confining pressure. For example, Lee [4] observed that the failure of specimens subjected to plane-strain biaxial compression (PBC) was always characterized by localized shear bands, whereas either localized or bulging diffuse failure mode could take place in CTC tests, depending on the density and the confining pressure level. Peters et al. [5] found that localized shear failures more often occur in sand under PBC loading, and bulging or diffuse failures are more commonly observed in CTC or CTE. Alshibli et al. [6] also reported that all their PBC tests ended up with localized failure characterized by well-developed conjugate shear bands whereas their CTC specimens showed bulging failure patterns.

Numerical simulations of failures in granular media have been commonly based on plasticity models and the finite element method (FEM), with a majority of them focusing on the 2D plane-strain case [7,8, among others]. These 2D studies indeed

* Corresponding author.
E-mail address: ceguo@connect.ust.hk (N. Guo).

http://dx.doi.org/10.1016/j.compgeo.2016.01.020
0266-352X/

successfully reproduce the formation and the development of shear band(s) which are consistent with experimental observations under the PBC condition. However, there have been rather limited numerical studies on the failure patterns of granular media under more general 3D loading conditions, and it is even more scarce for a comprehensive comparison of the macro–micro behavior in a granular material at failure under 2D and 3D conditions. Only a small handful of studies have made some attempts in this line. Based on FEM simulation of CTC tests on heterogeneous sands, for example, Andrade and Borja [9] investigated the influence of randomly distributed density on strain localization in sand. Andrade et al. [10] treated the CTC test on sand based on a multiscale approach where FEM with a simple two-parameter plasticity model was used to solve the boundary value problem (BVP) and the evolutions of the two model parameters were traced from a concurrently performed laboratory or discrete element method (DEM) test. A viscoplastic model was employed by Kodaka et al. [11] to simulate failures in saturated clay under the CTC loading using FEM where the effects of sample size were emphatically examined. Huang et al. [12] conducted a comprehensive bifurcation analysis of the failure modes under all CTC, CTE and PBC loading conditions and concluded that uniform bifurcation is more likely to occur in CTC tests and localized failure is more common in PBC and CTE tests. Notably, they have employed a special boundary condition (rigid pressure boundary) in their FEM simulations in conjunction with consideration of initial heterogeneity. Bifurcation analysis is typically based on a specific constitutive model and the characteristics of the acoustic tensor or the second-order work, and the approach has been followed by many other studies to identify the onset conditions of strain localization [13–16].

It is widely agreed today that key microscopic mechanisms underpin the dominant macroscopic behavior of a granular material. A thorough understanding of the failures in a granular material demands thus a robust modeling tool to provide simulations for both 2D and 3D loading conditions and meanwhile to be able to provide insights into the underlying microscopic mechanisms accounting for these failures. A 2D hierarchical multiscale approach has recently been developed by the authors [17–19] and has been successfully applied to simulate geotechnical engineering problems such as failure of retaining wall and footing [20] and to model the interplay between anisotropy and strain localization [21]. The approach will be extended in the present study to 3D to consider more realistic general loading conditions. While conceptually sharing certain similarities with the work by Andrade et al. [10], our approach features the use of DEM packings embedded into the Gauss integration points of the FEM mesh to derive the local material responses, which helps to totally bypass the need for phenomenological constitutive assumptions such as yielding and flow rules. These DEM packings are treated as representative volume elements (RVEs) which receive local boundary conditions from the FEM computations and return stress and tangent stiffness to FEM to solve a BVP. As demonstrated in Guo and Zhao [18,20], the approach is capable of reproducing complex material and structural responses of granular media including anisotropy, non-coaxiality, cyclic hysteresis and strain localization, and helps to bridge the micro and macroscopic modeling of granular media and enables effective cross-scale analyses. The current study constitutes a new development of the approach for general 3D modeling of granular media. It is also noted that similar multiscale approaches have been presented by Kaneko et al. [22], Miehe et al. [23], Nguyen et al. [24] and Li et al. [25], all of which however were developed in 2D only.

The study is organized as follows. The solution procedure and the formulation of the hierarchical multiscale approach are first described in Section 2. Section 3 gives the DEM model parameters and discusses the guideline to determine the proper RVE size. The simulation results and pertaining analyses of the CTC, CTE and PBC tests are presented in Section 4. Major conclusions are summarized in Section 5. For symbols and notations, vectors and tensors are denoted with boldface letters; '·' and ':' are the inner and the double contraction operators, respectively; '∇' and '$\nabla\cdot$' take the gradient and the divergence of a variable, respectively; 'tr' and 'dev' take the trace and the deviator of a tensor, respectively; '$\otimes$' is the dyadic operator.

2. Hierarchical multiscale model

Two open-source codes are coupled in the hierarchical multiscale approach — `Escript` [26] for the FEM computation and `YADE` [27] for the DEM computation. The FEM is employed to discretize the continuum domain of a BVP into FE mesh and to solve the governing equations over the discretized domain. A mesoscale discrete particle assembly is considered at each Gauss point of the FEM mesh which, after receiving boundary conditions from the FEM, is solved by DEM to derive the local constitutive response. The obtained material response is further passed onto the FEM for the global solution. Meanwhile, the DEM solutions in the multiscale approach can naturally reproduce the nonlinear, state/path-dependent shear responses observed for granular media. A brief introduction of the formulations and the solution procedure is summarized in the following.

2.1. FEM solver

A quasi-static mechanical problem is governed by the following equilibrium equation:

$$\nabla \cdot \boldsymbol{\sigma} + \rho \mathbf{b} = \mathbf{0} \tag{1}$$

where $\boldsymbol{\sigma}$ is the stress tensor, ρ is the bulk density of the material, and $\mathbf{b}$ is the body force (e.g. gravity). The variational form of Eq. (1) can be obtained by multiplying it with a test function $\delta\mathbf{u}$ and integrating them over the domain Ω with the help of the Gaussian theorem

$$\int_{\Omega} \nabla\delta\mathbf{u} : \boldsymbol{\sigma}\, d\Omega - \int_{\Omega} \rho\, \delta\mathbf{u}\cdot\mathbf{b}\, d\Omega = \int_{\Gamma_t} \delta\mathbf{u}\cdot\mathbf{t}\, d\Gamma_t \tag{2}$$

where $\mathbf{t}$ is the traction exerted on the Neumann boundary Γ_t. The discrete matrix form of Eq. (2) is readily obtained for a discretized FE domain

$$\mathbf{K}\mathbf{u} = \mathbf{R} \tag{3}$$

where $\mathbf{u}$ is the primary unknown displacement vector. The global stiffness matrix $\mathbf{K}$ is assembled from

$$\mathbf{K} = \int_{\Omega} \mathbf{B}^{\mathrm{T}}\mathbf{D}\mathbf{B}\, d\Omega \tag{4}$$

where $\mathbf{B}$ $(= \partial\mathbf{N}/\partial\mathbf{x})$ is the deformation matrix ($\mathbf{N}$ is the discretization function). $\mathbf{D}$ is the tangent modulus commonly used in solving a nonlinear problem. The residual force $\mathbf{R}$ in Eq. (3) is contributed by several terms per Eq. (2)

$$\mathbf{R} = \int_{\Omega} \mathbf{N}^{\mathrm{T}}\rho\mathbf{b}\, d\Omega + \int_{\Gamma_t} \mathbf{N}^{\mathrm{T}}\mathbf{t}\, d\Gamma_t - \int_{\Omega} \mathbf{B}^{\mathrm{T}}\boldsymbol{\sigma}^0\, d\Omega \tag{5}$$

where $\boldsymbol{\sigma}^0$ is the current (old) stress.

For a general nonlinear problem, Eq. (3) is frequently solved through Newton–Raphson iterations, by updating $\mathbf{K}$ and $\mathbf{R}$ with updated tangent modulus $\mathbf{D}$ and the stress tensor $\boldsymbol{\sigma}$ at the local Gauss points of the FE mesh. In the current study, both $\mathbf{D}$ and $\boldsymbol{\sigma}$ are homogenized from the RVE packings, as detailed in the following subsection.

2.2. DEM solver

In the hierarchical multiscale approach, a RVE packing is embedded to each Gauss point of the FEM mesh to derive the local material constitutive response. As schematically illustrated in Fig. 1, each RVE packing receives the local deformation $\nabla\mathbf{u}$ from the FEM solution as its boundary condition and is solved by the DEM solver. Based on the DEM solution, the local tangent operator $\mathbf{D}$ and the stress tensor $\boldsymbol{\sigma}$ are extracted and returned to the FEM which are then used in Eqs. (4) and (5) by the FEM solver.

The stress tensor for a RVE packing is homogenized based on the Love's formula

$$\boldsymbol{\sigma} = \frac{1}{V}\sum_{N_c} \boldsymbol{d}^c \otimes \boldsymbol{f}^c \tag{6}$$

where V is the volume of the RVE packing, N_c is the number of contacts within the packing, and $\boldsymbol{f}^c$ and $\boldsymbol{d}^c$ are the contact force and the branch vector joining the centers of the two contacted particles, respectively. An illustration of the interparticle contact is shown in Fig. 2. With the stress tensor, two commonly referred stress measurements—the mean stress p and the deviatoric stress q can be calculated

$$\begin{aligned} p &= -\frac{1}{3}\mathrm{tr}\boldsymbol{\sigma} \\ q &= \sqrt{\frac{3}{2}\mathrm{dev}\boldsymbol{\sigma} : \mathrm{dev}\boldsymbol{\sigma}} \end{aligned} \tag{7}$$

Note that $\boldsymbol{\sigma}$ in Eqs. (1) and (6) is defined positive for extension following the convention in solid mechanics and FEM computations. When presenting the results, we follow the convention in soil mechanics to treat compression as positive. For the strain measures, we obtain the strain tensor from the symmetric part of the displacement gradient $\boldsymbol{\varepsilon} = (\nabla\mathbf{u} + \nabla^{\mathrm{T}}\mathbf{u})/2$ and find the volumetric strain ε_v and the deviatoric strain ε_q accordingly

$$\begin{aligned} \varepsilon_v &= -\mathrm{tr}\boldsymbol{\varepsilon} \\ \varepsilon_q &= \sqrt{\frac{2}{3}\mathrm{dev}\boldsymbol{\varepsilon} : \mathrm{dev}\boldsymbol{\varepsilon}} \end{aligned} \tag{8}$$

The tangent operator can be estimated from the homogenized modulus of the discrete packing according to Wren and Borja [28] and Kruyt and Rothenburg [29]

$$\mathbf{D} = \frac{1}{V}\sum_{N_c}(k_n \boldsymbol{n}^c \otimes \boldsymbol{d}^c \otimes \boldsymbol{n}^c \otimes \boldsymbol{d}^c + k_t \boldsymbol{t}^c \otimes \boldsymbol{d}^c \otimes \boldsymbol{t}^c \otimes \boldsymbol{d}^c) \tag{9}$$

where $\boldsymbol{n}^c$ and $\boldsymbol{t}^c$ (see Fig. 2) are the unit normal and the tangential vectors at a contact, respectively. k_n and k_t are the normal and the tangential contact stiffnesses in the DEM model, respectively.

In the current study, a linear force–displacement contact law is assumed, where k_n and k_t are determined from two parameters E_c and v_c through

$$\begin{aligned} k_n &= E_c r^* \\ k_t &= v_c k_n \end{aligned} \tag{10}$$

where r^* $(= 2r_1r_2/(r_1 + r_2))$ is the common radius of the two contacted particles with radii r_1 and r_2, respectively. The contact normal force $\boldsymbol{f}_n^c$ and the tangential force $\boldsymbol{f}_t^c$ are then calculated

$$\begin{aligned} \boldsymbol{f}_n^c &= -k_n \delta \boldsymbol{n}^c \\ \boldsymbol{f}_t^c &= -k_t \boldsymbol{u}_t^c \end{aligned} \tag{11}$$

where δ is the overlap between the two contacted particles, and $\boldsymbol{u}_t^c$ is the relative tangential displacement at the contact. To reproduce the frictional interparticle contact behavior, a Coulombian threshold is imposed on the tangential force

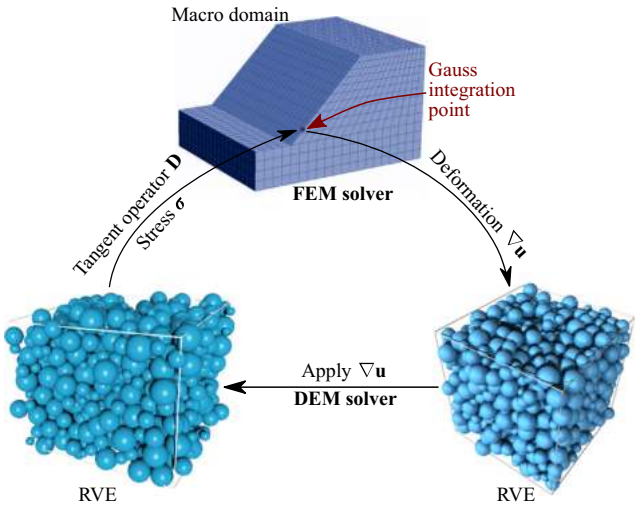

Fig. 1. Solution procedure of the hierarchical multiscale approach.

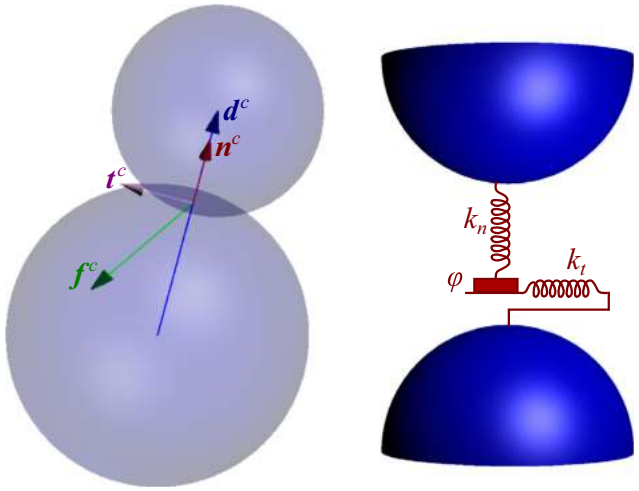

Fig. 2. Illustration of an interparticle contact.

$$|\boldsymbol{f}_t^c| \leqslant \tan\varphi |\boldsymbol{f}_n^c| \tag{12}$$

where φ is the interparticle friction angle. In addition to the interparticle contact force, a numerical damping, $\boldsymbol{f}^{\mathrm{damp}}$, is also assumed to dissipate the kinetic energy of the particles. The direction of $\boldsymbol{f}^{\mathrm{damp}}$ is opposite to the translational velocity of the particle $\boldsymbol{v}_p$ and its magnitude is proportional to the unbalanced force $\boldsymbol{f}^{\mathrm{unbal}}$ on the particle with a damping ratio α

$$\boldsymbol{f}^{\mathrm{damp}} = -\alpha |\boldsymbol{f}^{\mathrm{unbal}}| \boldsymbol{v}_p / |\boldsymbol{v}_p| \tag{13}$$

E_c, v_c, φ, α, along with the particle size distribution and particle density ρ_p are the general user defined parameters in the DEM model (see [27] for more detail).

Table 1
Parameters used in the DEM model.

Radii (mm)	ρ_p (kg/m^3)	E_c (MPa)	v_c	φ (rad)	α
2–6	265,000	600	0.8	0.5	0.1

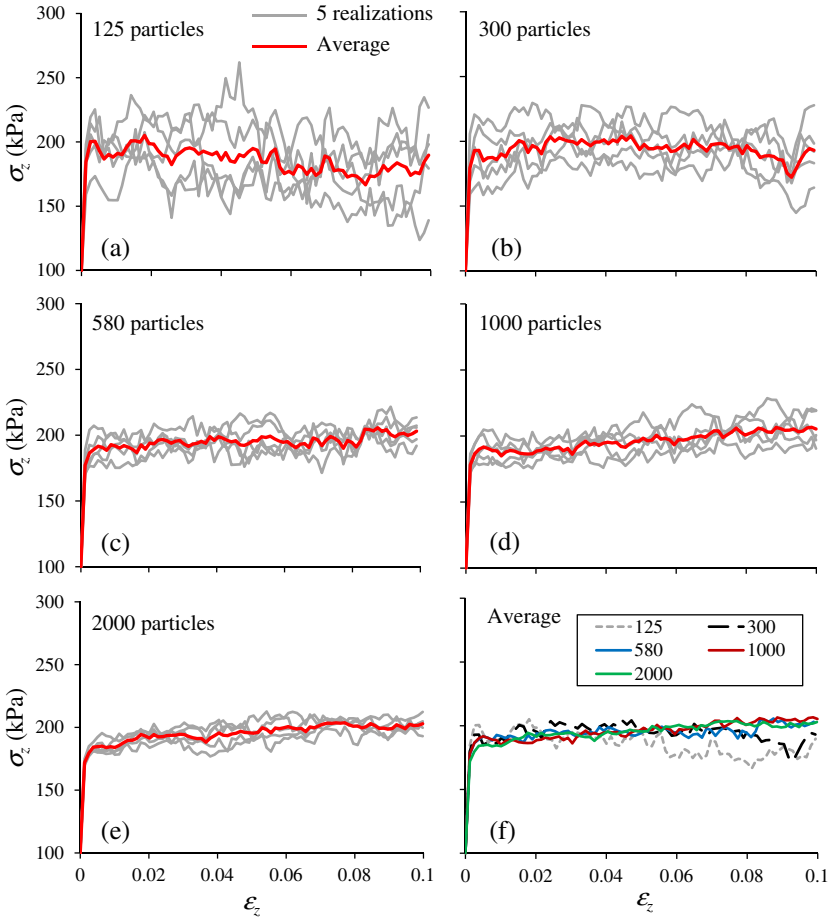

Fig. 3. Shear behaviors of RVEs with different sizes.

3. Selection of RVE size

The macroscopic responses of a granular medium are intrinsically governed by its microscopic properties, such as particle size distribution, interparticle contact and kinematics (sliding and rotation), and particle morphology (e.g. roundness, sphericity and roughness). The choice of a proper RVE is thus central to the hierarchical multiscale analysis. For a particular problem, these microscopic parameters should be carefully calibrated in the DEM model, for example, to benchmark some standard experimental data on sand. For convenience, the current study employs a simplified DEM model using spherical particles without considering rolling resistance, and adopts DEM model parameters which are typical in the literature, as listed in Table 1. The particle density ρ_p is scaled 100 times of the real value of silica sand grain in the study to accelerate the local DEM computations. It is proved to be a safe and efficient technique in simulating quasi-static problems [30]. Periodic boundary is used for the RVE, which satisfies the Hill–Mandel-type condition for energy conservation during scale transition [23].

Particular focus of the multiscale modeling is placed on the selection of the RVE, specifically, the proper RVE size or the sufficient number of particles to be considered for a RVE packing. While the size effect on strength for a heterogeneous material is well known, there is no widely agreed recommendation of RVE size for a granular material. The RVE size of a granular medium depends not only on the material itself (e.g. particle size distribution, density and pressure condition), but also on the structure sensitivity of the physical quantities under concern [31]. According to the definitions by Hashin [32] and Drugan and Willis [33], the RVE should be large enough to contain sufficient information about the microstructure and to accurately reproduce the overall modulus of the material. Meanwhile, it should be much smaller than the macroscopic body to prevent localization occurring inside the RVE. To determine the sufficient particle number in the RVE, we consider five different RVE sizes, containing 125, 300, 580, 1000 and 2000 particles, respectively. The particle size distribution and the material properties are the same as given in Table 1. Five realizations are randomly generated with different packing configurations for each RVE size. All packings (25 realizations in total) are then consolidated to the same initial void ratio $e_0 = 0.66$ and the same initial isotropic pressure $p_0 = 100$ kPa. Since the mechanical properties of the RVEs are concerned here, their shear responses under drained CTC loading (loaded in the z-direction, $\sigma_x = \sigma_y = 100$ kPa) are examined.

Fig. 3 shows a comparison among the different RVEs in terms of their stress–strain behaviors.[1] As can be seen, when the particle number is only 125 (Fig. 3(a)), the shear behavior for each realization shows great fluctuations. The deviations among different realizations are also large. With the increase of the particle number (Fig. 3(b)–(e)), the fluctuation is decreased and the deviation becomes narrower. This consistent trend unambiguously indicates that the shear behavior of a RVE packing gets increasingly stable and reliable when its particle number increases. By comparing Fig. 3(c), (d) and (e), we can see the shear behavior can be treated as stable when the particle number is larger than 580. The average responses of the three RVEs with 580, 1000 and 2000 particles are

[1] To differentiate the color used in plotting Figs. 3, 4, 11 and 14, the readers are referred to the web version of this article.

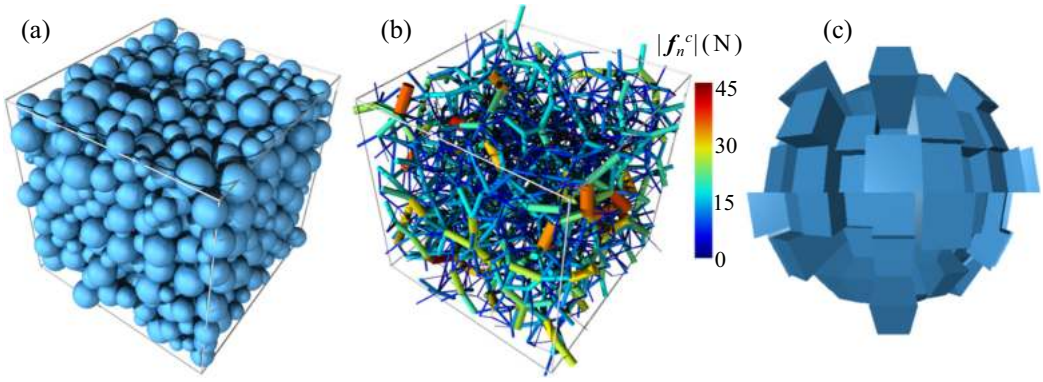

Fig. 4. (a) Prepared RVE packing and periodic cell; (b) force chain network; (c) contact normal distribution.

relatively smooth and very close to each other as seen from Fig. 3(f), whereas the average responses from the other two small RVEs are still fluctuated. Although the fluctuation and the deviation can be further reduced by increasing the RVE size and an ideal RVE should have negligible deviations among different realizations of an identical initial condition, we elect to use 1000 particles in our RVE for the following multiscale tests. As shown in the sequel, a typical multiscale triaxial test needs to handle millions of discrete particles in one simulation. The marginal improvement on the shear response by using more than 1000 particles in the RVE may well be overshadowed by the dramatically increased computational cost in terms of CPU time and memory demand. Therefore, a RVE with 1000 particles serves as a reasonable compromise between reliable RVE responses and affordable computational cost. Fig. 4 shows the final RVE adopted after isotropic consolidation ($e_0 = 0.528$, $p_0 = 100$ kPa). Note that a relatively dense packing of RVE are prepared in the study to facilitate the formation of shear band. In addition to the packing configuration in Fig. 4(a), the interparticle contact system is also presented in terms of the force chain network in Fig. 4(b) (chain width proportional to the magnitude of contact normal force) and the contact-normal based fabric tensor in Fig. 4(c), which is defined as [34]

$$\boldsymbol{\phi} = \int_{\Theta} E(\Theta)\boldsymbol{n}^c \otimes \boldsymbol{n}^c \, d\Theta = \frac{1}{N_c}\sum_{N_c} \boldsymbol{n}^c \otimes \boldsymbol{n}^c \tag{14}$$

where the distribution function $E(\Theta)$ can be approximated by a second-order Fourier expansion

$$E(\Theta) = \frac{1}{4\pi}[1 + \mathbf{F}_a : (\boldsymbol{n}^c \otimes \boldsymbol{n}^c)] \tag{15}$$

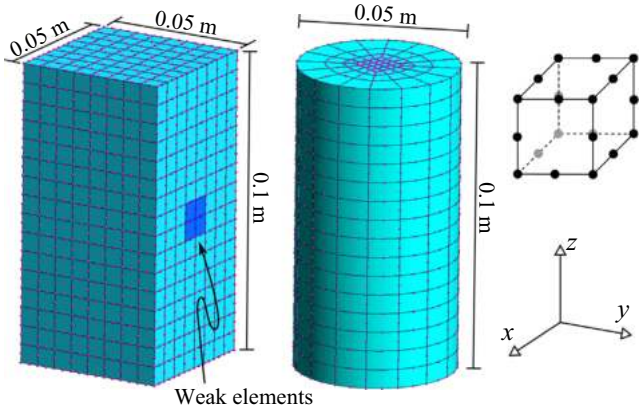

Fig. 5. Dimension and mesh for the cubical and the cylindrical specimens with the 20-node hexahedral element. The weak elements in the cubical specimen span from $y = 0$ m to $y = 0.05$ m.

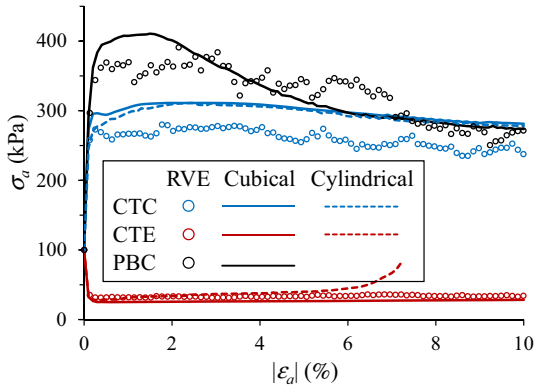

Fig. 6. Evolution of the resultant axial stress for the uniform specimens (without weak elements).

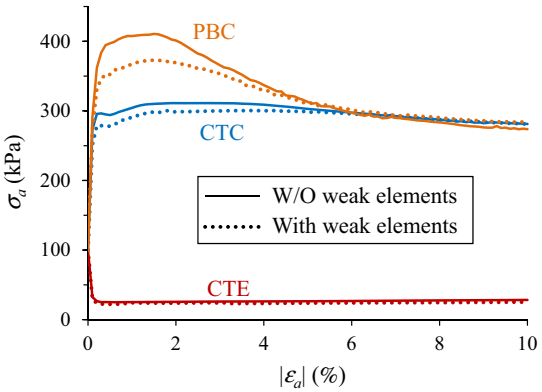

Fig. 7. Comparison of the resultant axial stress for the cubical specimen with or without weak elements.

where $\mathbf{F}_a$ ($= 15/2\mathrm{dev}\boldsymbol{\phi}$) is the deviatoric fabric tensor, whose anisotropic intensity can be characterized by a scalar $F_a = \sqrt{3/2\mathbf{F}_a : \mathbf{F}_a}$ [35]. The fabric tensor provides a convenient tool to characterize the internal structure of granular media under mechanical loading. As shown in Fig. 4, the initial RVE is roughly isotropic as the force chain is relatively homogeneous and the contact normal distribution is largely uniform.

4. 3D loading tests

Due to the hierarchical structure of the multiscale approach, the RVE packings at the Gauss points of the FE mesh can be solved by

DEM independently, which renders it straightforward to implement the parallel computing technique to speed up the multiscale modeling. We have implemented a message passing interface (MPI) [36,37] in our code to run separate DEM computations in parallel on a high-performance computing (HPC) cluster. A typical test presented in this section costs about 24 h using 4 HP ProLiant SL250 Gen8 nodes (each with 2×10-core 2.2 GHz CPU and 8×8 GB RAM) on a local cluster. As one such simulation involves millions of discrete particles for the whole problem domain, the performance demonstrates the multiscale approach is more efficient than the regular DEM. Indeed, an almost linear scalability can also be observed from the parallel computing scheme.

Two specimens with typical shapes in laboratory element tests, cubical and cylindrical, are chosen to perform the 3D loading tests. The heights of both specimens are 0.1 m. The cubical specimen has a square cross-section with a side length of 0.05 m, and the cylindrical specimen has a diameter of 0.05 m. FE meshes for the two specimens are shown in Fig. 5. Both specimens are discretized into 1024 20-node hexahedral elements using `Gmsh` [38]. Note that a similar discretization has been used by Andrade and Borja [9]. A reduced integration scheme, involving 8 Gauss points for each element, is adopted in the FEM computation (see also [11]). As a result, the multiscale computation for each specimen involves a total of 8192 RVE packings. With 1000 particles for every RVE,

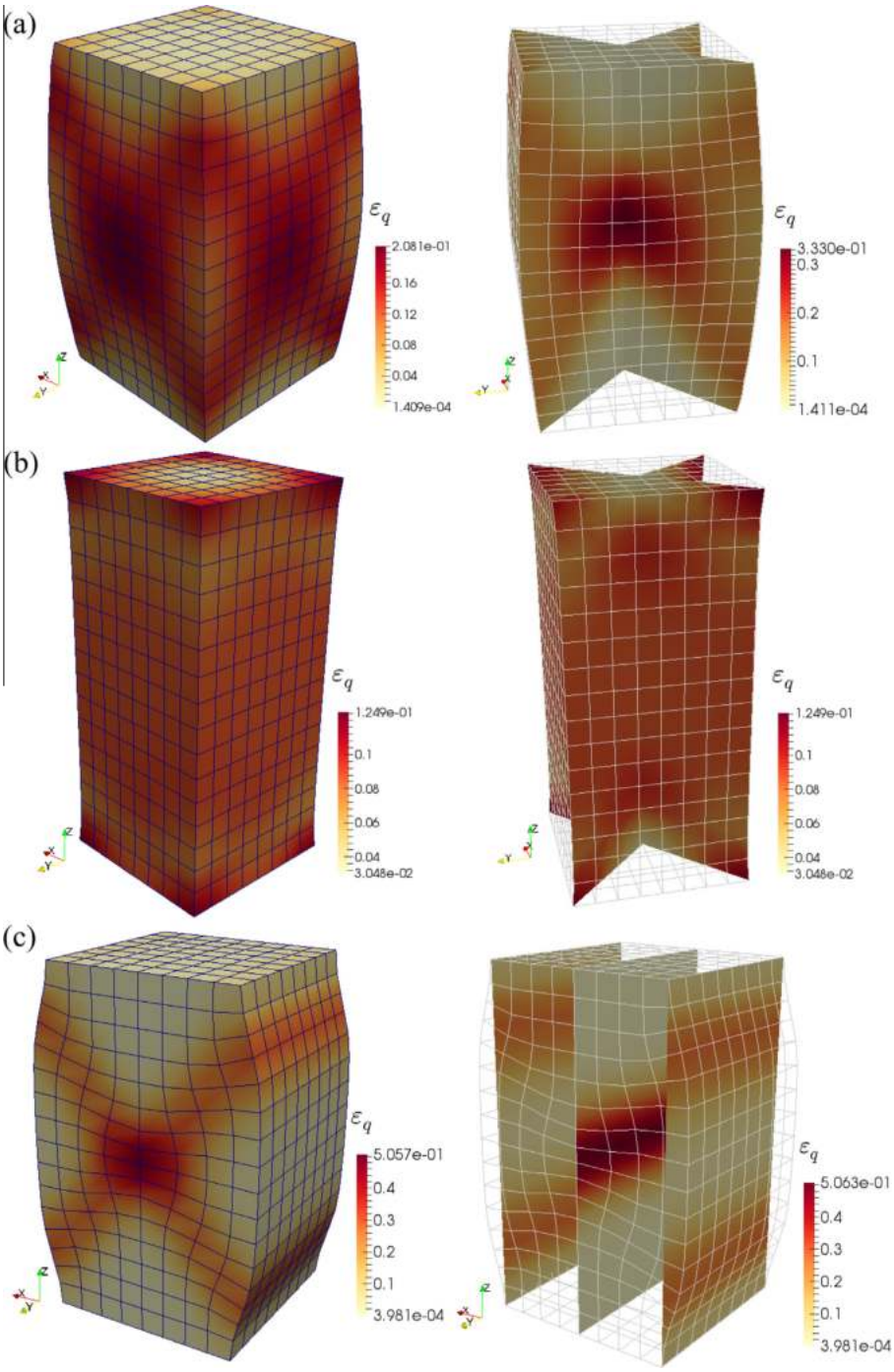

Fig. 8. Contours of shear strain for the uniform cubical specimen under the (a) CTC; (b) CTE and (c) PBC conditions at the final loading stage ($|\varepsilon_a| = 10\%$).

the total number of particles involved amounts to over 8 million. Three loading conditions, including the CTC, the CTE, and the PBC, are performed. In all testing cases, the bottom surface of the specimen is fixed, while the top surface is assumed rough, which means there are no lateral displacements allowed for nodes on the top surfaces. Uniform vertical displacements are then applied on these top-surface nodes to load the specimens axially. In CTC and CTE, a constant lateral confining pressure of 100 kPa is applied on the vertical surfaces of the specimen. In PBC (adapted from the cubical specimen), the displacements in the y direction are restricted for the nodes on the two outer surfaces at $y = 0$ m and $y = 0.05$ m, respectively. The confining pressure is only applied on the other two vertical surfaces (at $x = 0$ m and $x = 0.05$ m) of the specimen. An extra cubical specimen with preset weak elements in the central height spanning from $y = 0$ m to $y = 0.05$ m (see Fig. 5, left) is also examined under the three loading conditions. The weak elements are generated by assigning slightly loose RVE packings (initial void ratio $e_0 = 0.707$, the same to other RVE packings otherwise) to their Gauss points. Gravity is not considered in all tests (i.e. $\mathbf{b} = \mathbf{0}$ in Eq. (1)).

4.1. Stress–strain responses

The nominal axial stress–strain responses of the uniform specimens without preset weak elements are shown in Fig. 6. The nominal axial stress is calculated from the total force exerted on the top surface normalized by the area of the top surface. The responses of the RVE packing under the same conditions from separately performed pure DEM tests are also provided (shown as open circles) for comparison. Evidently, the PBC test gives a higher peak axial stress σ_a than the CTC test (411 kPa versus 311 kPa). The softening in the PBC test is also more significant and occurs at a much smaller axial strain ε_a than in the CTC one (1.5% versus 2.5%). These observations are in good agreement with those from experiments [4,39]. In the PBC test, the peak σ_a from the multiscale simulation is slightly higher than that from the RVE response, which is similar to the 2D plane-strain tests [21] and is attributed by the extra constraint imposed by the rough boundary condition. However, the post peak and the residual σ_a are rather similar between the multiscale result and the RVE response, albeit the latter is relatively fluctuated. Different from the PBC test, the RVE axial stress in the CTC test is always smaller than the multiscale result after the initial yield point. The difference in the two loading conditions is caused by their different failure modes as to be explained in Section 4.2. It is also seen that generally σ_a in the cylindrical specimen is marginally smaller than that in the cubical specimen. The difference is only noticeable at around the yield point ($\varepsilon_a \approx 0.25\%$). In the CTE test, the axial stress decreases dramatically to a minimum at $\varepsilon_a = -0.3\%$ due to the extension. The minimum σ_a from the RVE response is slightly larger than that from the multiscale simulation. Starting from that point, σ_a gradually increases and reaches a roughly constant value of 26 kPa in the cubical specimen, but it

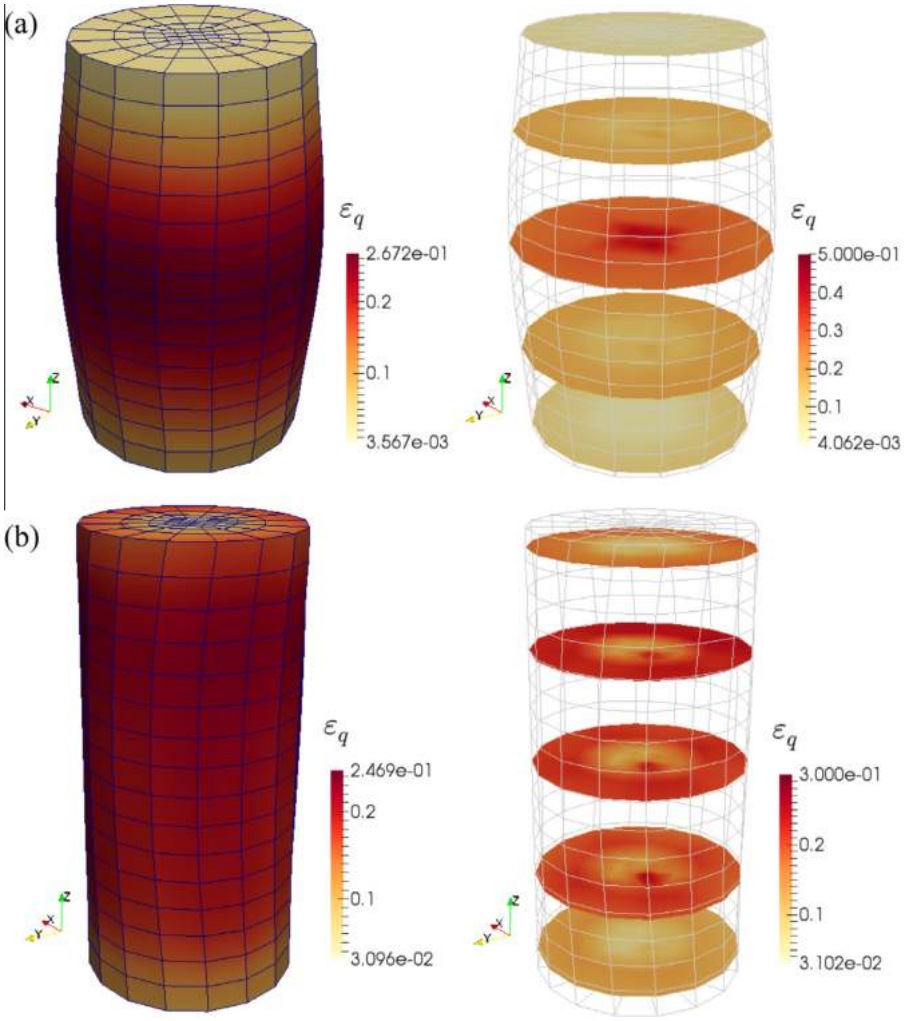

Fig. 9. Contours of shear strain for the uniform cylindrical specimen under the (a) CTC and (b) CTE conditions at the final loading stage ($\varepsilon_a = 10\%$ and -7.2% respectively).

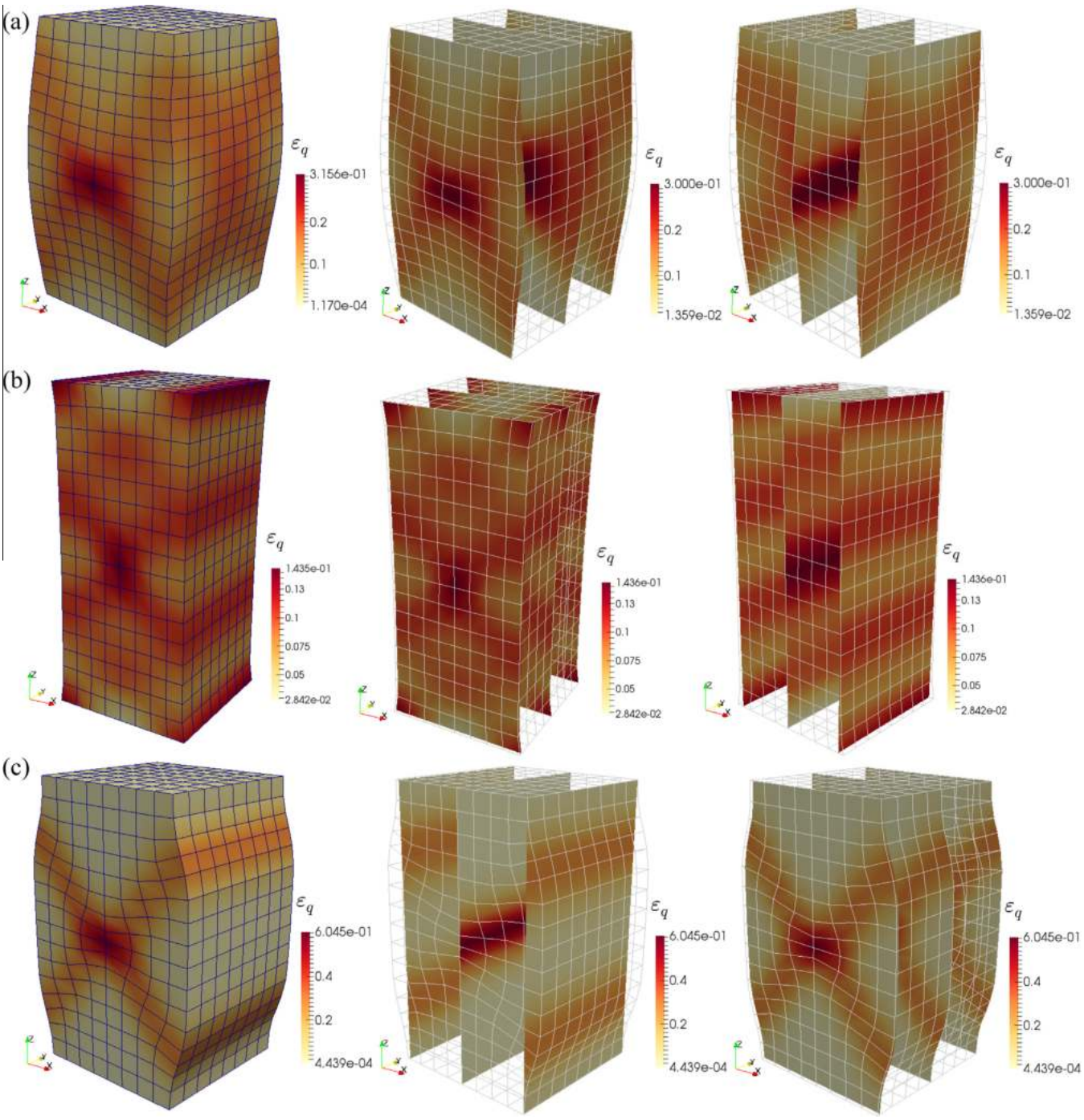

Fig. 10. Contours of shear strain for the imperfect cubical specimen (with weak elements) under the (a) CTC; (b) CTE and (c) PBC conditions at the final loading stage ($|\varepsilon_a| = 10\%$).

increases steadily in the cylindrical case. While the test on the cubical specimen still gives a reasonable result compared with the RVE response in the CTE test, the boundary condition for the confining pressure on the cylindrical specimen is more complex and easily becomes ill-posed. The cylindrical specimen has been found to become severely distorted at the point of $\varepsilon_a = -7.2\%$ (Section 4.2), which forces the termination of the computation at this point.

The behaviors of the imperfect cubical specimen (with preset weak elements) are compared in Fig. 7. Generally, their behaviors are almost the same before the initial yield point and at the late residual state compared with the behaviors of the uniform cubical specimen. Nevertheless, the imperfect specimen gives a smaller peak σ_a in the CTC and PBC tests and also a smaller valley σ_a in the CTE test than their corresponding uniform cases. The difference is the largest in the PBC condition and is intermediate in the CTC case. The difference observed in the CTE test is negligibly small.

4.2. Strain localization

This subsection presents a comparison of the different failure patterns observed in the multiscale simulations of specimens under various loading conditions. Fig. 8 shows the contours of the accumulated shear strain ε_q at the final stage ($|\varepsilon_a| = 10\%$) for

the uniform cubical specimen under different loading conditions. Under the CTC condition, a 3D localized zone has been observed. The emergences of the shear zone onto the x–z and y–z surfaces both show cross-shaped shear bands (Fig. 8(a, left)), which are similar to that observed in an early 2D plane-strain simulation [21]. From the vertical diagonal slices of the specimen (Fig. 8(a, right)), it is found the most severe localization occurs at the inner-center of the specimen (maximum $\varepsilon_q = 0.33$ at the inner-center and 0.21 on the surface) and the shear zone extends from the inner-center to the eight corners of the specimen. A similar 3D shear zone of the octopus shape has also been observed by the simulation of Kodaka et al. [11] for water-saturated clay. In contrast, under the CTE condition, a diffuse failure with no obvious localization has been observed (Fig. 8(b)). The specimen deforms relatively uniformly except at the boundary areas where boundary effects play a role. The maximum shear strain ($\varepsilon_q = 0.12$) is also small compared to that in CTC test (which actually occurs at the corner of the specimen where the boundary effect is the strongest). Different from the CTC and the CTE conditions, a pair of cross-shaped conjugate planar shear bands (Fig. 8(c, left)) can be clearly identified under the PBC condition which is commonly seen in 2D plane-strain experiments and simulations. In contrast to the cross-shaped shear bands on the x–z plane, one (only at the near-center cross-sections) or two horizontal bands can be observed on the y–z plane (Fig. 8(c, right)). From Fig. 8(a), (b) and (c), it is concluded that shear localized failure is easier to develop in the PBC condition, where the shear zone is more appreciably concentrated within a narrow band and the maximum shear strain is much larger ($\varepsilon_q = 0.51$ in PBC versus 0.33 in CTC and 0.12 in CTE). The localized failure is difficult to initiate in the CTE condition where diffuse failure takes place instead.

Similarly, the cylindrical specimen has been subjected to the CTC and the CTE tests. The contours of the accumulated shear strain at the final stage are presented in Fig. 9. For the CTC condition, instead of the shear localized failure found on the cubical specimen, an obvious bulging failure occurs for the cylindrical specimen (Fig. 9(a, left)). As the shape becomes axisymmetric, the specimen appears to be more resistant to localized failure. However, similar to the cubical specimen, the maximum shear strain is observed at the inner-center of the specimen, as can be seen from the horizontal slices (Fig. 9(a, right)). Due to the constraints at the top and the bottom surfaces, the bulging is also most severe at the center height of the specimen. These observations agree qualitatively well with some experiments using X-ray computed tomography [40,41]. Again for the CTE test, the specimen fails diffusively and the deformation is relatively uniform inside the specimen (Fig. 9(b, left)). However, from the horizontal slices, it is found the shear intensity is larger in the outer part than in the inner part of the specimen (Fig. 9(b, right)). In addition, a noticeable twisting of the entire specimen is observed, which explains the increase of the axial stress shown in Fig. 6. By comparing Figs. 8 and 9, we can see that at the same aspect ratio, the specimens with different shapes of the cross-section can have different failure modes.

In the above analyses, the specimens are prepared to be initially uniform, with all Gauss points being assigned with identical RVE packings. In nature, however, a specimen is usually inhomogeneous due to randomness, e.g. the distributed density and the micro-structure. The inhomogeneity or the imperfection can also exert a profound influence on the strength and the failure pattern of a specimen [9]. In this study, the imperfection is simplified to a row of weak elements embedded into the cubical specimen (see Fig. 5). It is noted random RVE packings can also be assigned to the Gauss points across the domain to generate the imperfection, which may make the specimen more realistic but nevertheless is not attempted in the present study. The failure patterns of the imperfect cubical specimen under different loading conditions are shown in Fig. 10. As the embedded weak elements break the symmetry of the x–z and the y–z planes, under the CTC condition, the strain localization is more distinct in the x–z plane than in the y–z plane (Fig. 10(a, left)), which differs from the uniform specimen. However, there are vague crossed shear bands seen in the

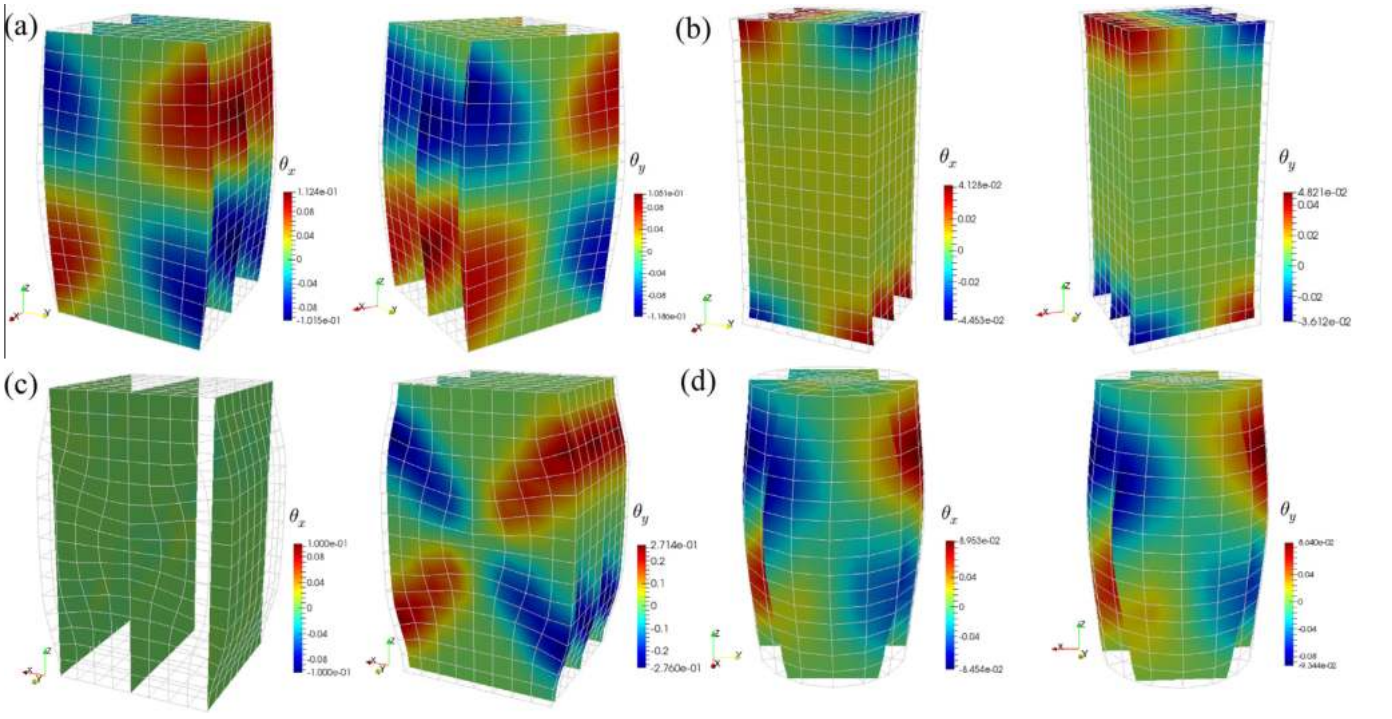

Fig. 11. Contours of accumulated average particle rotation for the uniform (a) CTC cubical; (b) CTE cubical; (c) PBC cubical and (d) CTC cylindrical specimens at the final loading stage ($|\varepsilon_a| = 10\%$).

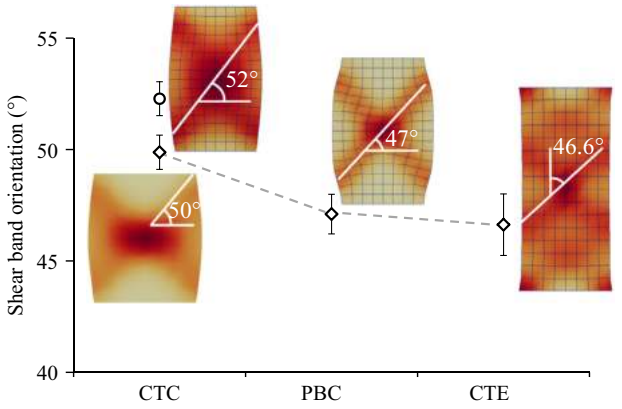

Fig. 12. Orientation of shear band with respect to the minor stress direction under different loading conditions.

outer y–z slices and there is a distinctive horizontal band in the center height of the inner y–z slice (Fig. 10(a, right)), whose position corresponds to that of the weak elements. An apparently different failure mode under the CTE condition has been observed for the imperfect specimen compared with its uniform counterpart case. Instead of diffuse failure in the previous uniform case, localized failure takes place. Three pairs of crossed conjugate planar shear bands can be identified in the x–z plane, among which the one intersecting at the weak elements is most distinct (Fig. 10(b, left and middle)). The effect of the weak elements is even stronger in the CTE condition than in the CTC one. Only horizontal bands (4 for the outer slices and 3 for the inner one) can be observed in the y–z slices (Fig. 10(b, right)). The shear band pattern of the imperfect specimen under the PBC condition is rather similar to that of the uniform specimen (Fig. 10(c)). With the embedded weak elements, the maximum shear strain increases under all loading conditions.

In addition to the shear strain contour, X-ray computed tomography [42] and DEM simulations [43] reveal that significant particle rotation takes place within shear localized zones. This has also been demonstrated in our previous 2D multiscale simulations [20,21]. The accumulated average particle rotation $\boldsymbol{\theta}$ for a RVE packing is defined as

$$\boldsymbol{\theta} := (\theta_x, \theta_y, \theta_z)^{\mathrm{T}} = \frac{1}{N_p}\sum_{N_p}\boldsymbol{\theta}^p \tag{16}$$

where N_p is the number of particles, $\boldsymbol{\theta}^p$ is the accumulated rotation of an individual particle. The contours of $\boldsymbol{\theta}$ projected onto the vertical planes for the uniform specimens at the final loading stage are shown in Fig. 11. For the cubical specimen under the CTC condition, a similar fourfold pattern is observed on both the y–z (θ_x, Fig. 11(a, left)) and x–z (θ_y, Fig. 11(a, right)) planes. Looking from the positive x (or y) to the negative x (or y) axis, we observe positive (shown in red for anti-clockwise rotation) θ_x (or θ_y) at the top-right and the bottom-left quarters but negative (shown in blue for clockwise rotation) θ_x (or θ_y) at the top-left and the bottom-right quarters of the y–z (or x–z) plane. This pattern is close to that observed from 2D simulations, indicating crossed shear bands on these two vertical planes. But unlike the slim bands in 2D test [21], the localized zones appear to be round and fat. For the cubical specimen under the CTE condition, except at the top and the bottom ends, the domain is relatively uniform with almost zero average particle rotation on both y–z and x–z planes (Fig. 11(b)), which is consistent with the diffuse failure pattern found in Fig. 8(b). Indeed, even close to the boundary constraints, the rotation magnitude is relatively small (maximum $|\theta| \approx 0.04$). The PBC test shows a rather similar pattern on the x–z plane (Fig. 11(c, right)) to that of a 2D plane-strain test, with well developed cross-shaped conjugate planar shear bands. The magnitude of average particle rotation inside the localized zones is much larger ($|\theta| \approx 0.3$) than the other cases. In contrast, the particles have almost zero rotation on the y–z plane (Fig. 11(c, left)) even inside the horizontal bands seen in Fig. 8(c, right). For the cylindrical specimen under the CTC condition (Fig. 11(d)), a localized pattern similar to that in the cubical specimen under the same CTC condition (Fig. 11(a)) is observed, which is a rather surprising finding as the specimen is found undergoing

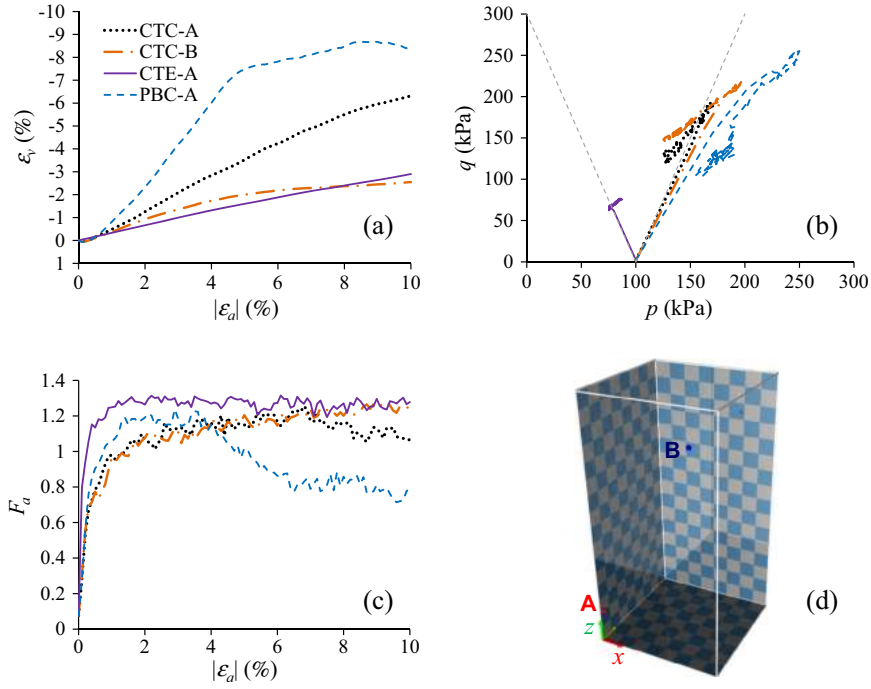

Fig. 13. Responses of the selected points of the uniform cubical specimen under different loading conditions: (a) dilation; (b) loading path; (c) fabric anisotropy; (d) location of the selected points.

a bulging failure from the shear strain contour (Fig. 9(a)). However, the contour of $\boldsymbol{\theta}$ suggests that shear localization, perhaps less dominant than bulging, also develops inside the specimen. Not presented here, the contour of the cylindrical specimen under the CTE condition has a similar diffuse pattern to that of the cubical specimen (Fig. 11(b)) before severe distortion occurs. One further remark on the average particle rotation defined in Eq. (16) is that $\boldsymbol{\theta}$ is more representative of the global rotation of the RVE (Fig. 14 (d, left)). The rotation of individual particles inside the shear bands, although has large magnitudes, may experience different directions [44,45].

The orientation of shear band under the different loading conditions is further examined. Fig. 12 shows the orientation angle of the shear band measured with respect to the minor stress direction of the specimens (horizontal in CTC and PBC, vertical in CTE). Since planar shear bands are observed in the PBC and the CTE tests (Figs. 8(c), 10(b) and (c)), the angles under the two test conditions are measured from the surface of the specimens. While localization in the CTC test forms a 3D octopus-shaped zone, the angle of shear band is estimated from both the surface and the vertical diagonal planes. It is found from Fig. 12 that the angle on the surface plane is larger than that on the vertical diagonal plane, the latter of which is deemed more appropriate for the angle of the 3D shear localized zone. A decreasing trend is also observed from CTC to PBC and to CTE, which suggests the shear band angle decreases with the increase of the intermediate principal stress ratio. Nevertheless, the drop from PBC to CTE is marginally small.

4.3. Multiscale analysis

A prominent feature of the hierarchical multiscale approach is its capacity in providing direct macro–micro bridging for granular media. To demonstrate this, two Gauss points of the uniform cubical specimen, as shown in Fig. 13(d), are selected, where Point A (coordinate = $(0.0013, 0.0013, 0.0138)^{\mathrm{T}}$) is located inside the shear localized zone for the CTC and the PBC tests and Point B (chosen for CTC test only, coordinate = $(0.0263, 0.0263, 0.0763)^{\mathrm{T}}$) is outside the localized zone. The dilation responses, the loading paths and the evolutions of fabric anisotropy of the two points are plotted in Fig. 13(a)–(c). In the CTC test, Point A undergoes a large deformation with significant dilation (ε_v reaches -6.33%), whereas Point B undergoes a small deformation with mild dilation (ε_v reaches

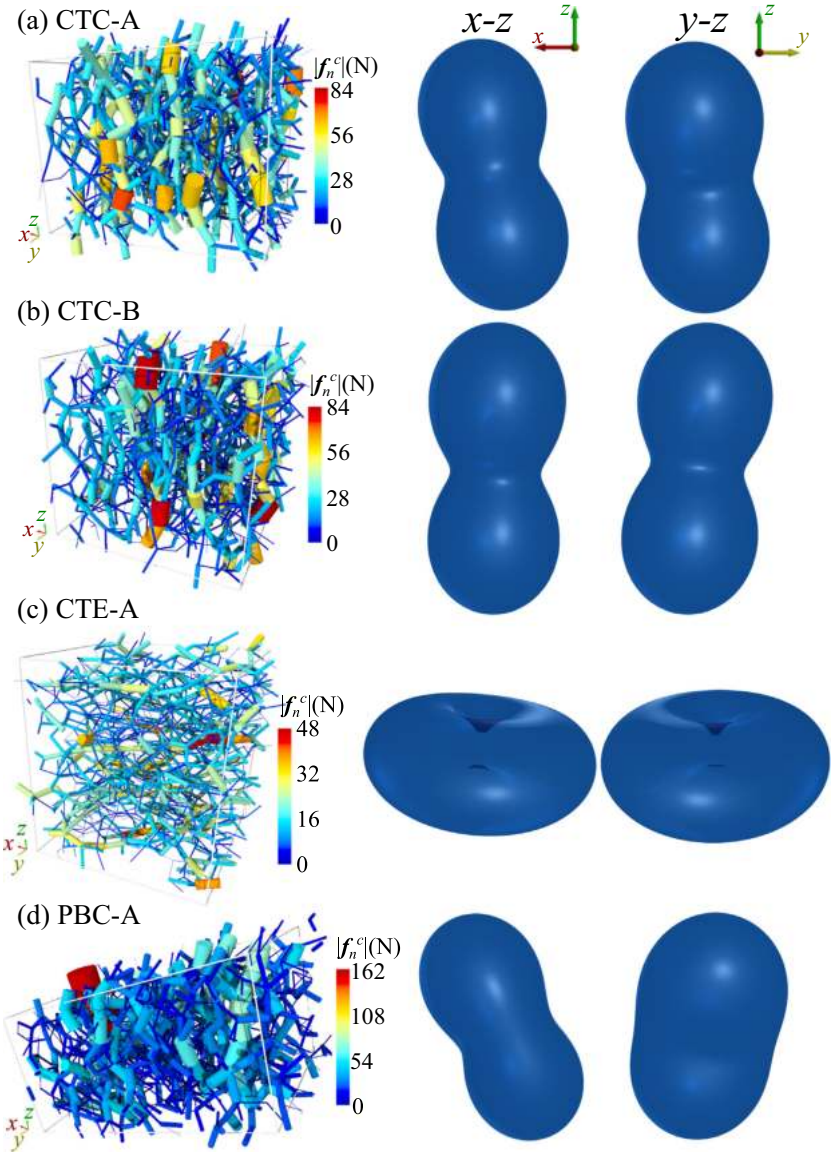

Fig. 14. Force chain network and fabric of the selected points of the uniform cubical specimen at the final loading stage.

−2.55%). Nevertheless their loading paths are close to each other, both following approximately a CTC loading path ($\Delta q/\Delta p = 3$). Their post-peak stress paths show strong fluctuations for both points. The fabric anisotropy shows similar evolutions for the two points under CTC. However, there is a mild decrease in F_a after $\varepsilon_a = 6.8\%$ for Point A, whereas at Point B F_a increases steadily. For the same point A under different loading conditions, the dilation is most significant under PBC loading (ε_v reaches −8.7%). The evolution of dilation under CTE loading is almost linear (without initial contraction which is observed for other loading conditions) as the overall deformation is relatively uniform for the CTE test. The slope of the loading path ($\Delta q/\Delta p$) is −3 for CTE and slightly less than 3 for PBC. An obvious stress softening is observed for the PBC test from its loading path (peak $q = 255$ kPa, residual $q = 118$ kPa), which is consistent to the overall softening of the specimen plotted in Fig. 6. The fabric anisotropy of Point A under CTE increases faster than under CTC and PBC, and is generally larger. This is because the confining pressure level is lower for CTE condition than the other two conditions, which could render the contact force network more anisotropic [35,46]. The F_a of Point A under CTE reaches a steady value after $\varepsilon_a = -1\%$, whereas the F_a under PBC experiences a drastic decrease after $\varepsilon_a = 3.5\%$.

It is instructive to examine the microstructure of the two points under different loading conditions. Fig. 14 presents the force chain network and the homogenized fabric (using Eq. (15)) of the two points at the final loading stage. Under the CTC loading, both Point A and B possess a highly anisotropic structure. Strong force chains are found roughly aligned in the vertical direction. The force magnitudes are comparable for these two points. The smoothed distribution of the contact normals has a dumb-bell shape, whose major axis tilts slightly from the vertical direction. From the projections on the x–z and the y–z planes, it is also seen the two points are roughly isotropic in the x–y plane under the CTC loading. By comparing Figs. 13(b) and (c) and 14(a) and (b), the stress level, the contact force network and the fabric anisotropy of the two points (one inside and the other outside the shear localized zone) appear to differ insignificantly. Therefore, the contour of the stress or the contact normal based fabric anisotropy cannot be used to identify the shear localized zone [18,21]. For Point A under the CTE loading, strong force chains are found aligned horizontally. The smoothed distribution of the contact normals looks like a donut or a red blood cell with major axes in the horizontal plane. The contact force magnitude in CTE is generally smaller than that in CTC. Under the PBC condition, Point A undergoes a significant anti-clockwise rotation on the x–z plane seen from the positive y-axis, which is consistent with the observation in Fig. 11(c). Except one exceptionally large force chain, the average force magnitude of Point A under PBC is comparable to that under CTC. Indeed, Point A experience a similar stress level under the two conditions as seen from Fig. 13(b). The smoothed distribution of the contact normals presents a dumb-bell shape on the x–z projection, whose major direction, however, is oblique from the vertical direction due to the rotation of the RVE packing. on the y–z plane, the smoothed distribution of the contact normals has a potato-like shape, suggesting the y-direction possesses the second-most interparticle contacts under the PBC loading.

5. Conclusions

A 3D hierarchical multiscale approach has been presented to investigate strain localization under three typical loading conditions: CTC, CTE and PBC. While providing a robust alternative to conventional phenomenological approaches in modeling granular media and relevant BVPs, the proposed approach offers a straightforward means to establish the macro–micro relationship towards a deeper understanding of the behavior of granular media. The multiscale modeling of strain localization in granular media leads to the following major findings, among the three loading conditions:

(a) The PBC testing condition gives rise to the highest peak nominal axial stress as well as the most significant softening response, which agrees with the experimental observations [4,39]. The CTC and the CTE tests on the cubical and the cylindrical specimens give similar nominal axial stresses. The inhomogeneous specimen (with preset weak elements) has smaller peak stresses than the uniform specimen, but with close residual stresses.
(b) The cubical specimen develops an octopus-shaped shear localized zone under CTC and two crossed planar shear bands under PBC, whereas it fails in diffuse mode under CTE. The cylindrical specimen undergoes a bulging failure under the CTC loading condition, and a distorted diffuse failure under CTE. The weak elements facilitate the formation of localized failure for the cubical specimen under the CTE loading condition.
(c) The contour of average particle rotation is a good indicator for strain localization. The particles inside the shear localized zone experience much more severe rotation than those outside the localized region. From the contour of average particle rotation, shear localization is also found for the cylindrical specimen under the CTC loading, although bulging failure is observed from the outer surface of the specimen. The shear band orientation (with respect to the minor stress direction) shows a decreasing trend from the CTC to the PBC to the CTE loading conditions (with increasing of the intermediate principal stress ratio).
(d) The multiscale approach enables a cross-scale analysis of the strain localization problem. The dilation is large for the point inside the shear localized zone and it is mild for the point outside the localized zone. However, there are no big difference in the stress level, the interparticle force magnitude and the contact normal based fabric anisotropy for points inside and outside the localized zone, which suggests these quantities may not be well suited for identifying the shear localized zone as compared to other quantities such as shear strain, density or average particle rotation. The fabric anisotropy presents different shapes under different loading conditions.

There are also some limitations of the current approach. The material response is captured by the local RVE packing and the RVE needs to be carefully chosen for a particular problem. DEM commonly adopts simplified models to describe sand grains and their interactions, quantitative modeling of real sand behavior, at this stage, still requires some undesired phenomenological calibration of the DEM model, e.g. by adding rolling resistance. Faithful modeling of particle shape is a continuous pursuit of the authors' group towards possible improvements in this regard [47–49]. The second issue lies in the computational efficiency. As a full 3D simulation involves millions of particles, the computational cost is considerable. Although parallel computing techniques adopted in the current study help to relieve certain burden, the algorithms in both the DEM (e.g. accelerating interparticle contact detection) and the FEM (e.g. using more efficient tangent operator) computations need to be further optimized for practical application of the proposed multiscale approach.

Acknowledgments

The study is supported by Research Grants Council of Hong Kong through GRF No. 623211 and University Grants Committee through a theme-based project No. T22-603/15-N. We also

acknowledge the financial support of two Research Equipment Competition grants 2011–12 and 2013–14 at HKUST on the HPC cluster which was used for the computation.

References

[1] Uthayakumar M, Vaid YP. Static liquefaction of sands under multiaxial loading. Can Geotech J 1998;35:273–83.
[2] Yoshimine M, Ishihara K, Vargas W. Effects of principal stress direction and intermediate principal stress on undrained shear behaviour of sand. Soils Found 1998;38(3):179–88.
[3] Griffiths DV, Marquez RM. Three-dimensional slope stability analysis by elasto-plastic finite elements. Géotechnique 2007;57(6):537–46.
[4] Lee K. Comparison of plane strain and triaxial tests on sand. J Soil Mech Found Divis 1970;96(3):901–23.
[5] Peters J, Lade P, Bro A. Shear band formation in triaxial and plane strain tests. In: Donaghe R, Chaney R, Silver M, editors. Advanced triaxial testing of soil and rock, ASTM, STP977. ASTM; 1988. p. 604–27.
[6] Alshibli KA, Batiste SN, Sture S. Strain localization in sand: plane strain versus triaxial compression. J Geotech Geoenviron Eng 2003;129(6):483–94.
[7] Tejchman J, Wu W. Non-coaxiality and stress–dilatancy rule in granular materials: FE investigation within micro-polar hypoplasticity. Int J Numer Anal Methods Geomech 2009;33:117–42.
[8] Gao Z, Zhao J. Strain localization and fabric evolution in sand. Int J Solids Struct 2013;50:3634–48.
[9] Andrade JE, Borja RI. Capturing strain localization in dense sands with random density. Int J Numer Methods Eng 2006;67:1531–64.
[10] Andrade J, Avila C, Hall S, Lenoir N, Viggiani G. Multiscale modeling and characterization of granular matter: from grain kinematics to continuum mechanics. J Mech Phys Solids 2011;59:237–50.
[11] Kodaka T, Higo Y, Kimoto S, Oka F. Effects of sample shape on the strain localization of water-saturated clay. Int J Numer Anal Methods Geomech 2007;31:483–521.
[12] Huang W, Sun D, Sloan SW. Analysis of the failure mode and softening behaviour of sands in true triaxial tests. Int J Solids Struct 2007;44:1423–37.
[13] Rudnicki JW, Rice JR. Conditions for the localization of deformation in pressure-sensitive dilatant materials. J Mech Phys Solids 1975;23(6):371–94.
[14] Vardoulakis I, Goldscheider M, Gudehus G. Formation of shear bands in sand bodies as a bifurcation problem. Int J Numer Anal Methods Geomech 1978;2:99–128.
[15] Bigoni D, Zaccaria D. On strain localization analysis of elastoplastic materials at finite strains. Int J Plasticity 1993;9:21–33.
[16] Nicot F, Darve F, Khoa HDV. Bifurcation and second-order work in geomaterials. Int J Numer Anal Methods Geomech 2007;31:1007–32.
[17] Guo N, Zhao J. A hierarchical model for cross-scale simulation of granular media. In: AIP conference proceedings, vol. 1542; 2013a. p. 1222–5.
[18] Guo N, Zhao J. A coupled FEM/DEM approach for hierarchical multiscale modelling of granular media. Int J Numer Methods Eng 2014;99(11):789–818.
[19] Guo N. Multiscale characterization of the shear behavior of granular media. Ph. D. thesis, The Hong Kong University of Science and Technology, Hong Kong; 2014.
[20] Guo N, Zhao J. Multiscale insights into classical geomechanics problems. Int J Numer Anal Methods Geomech 2016;40(3):367–90.
[21] Zhao J, Guo N. The interplay between anisotropy and strain localisation in granular soils: a multiscale insight. Géotechnique 2015;65(8):642–56. http://dx.doi.org/10.1680/geot.14.P.184.
[22] Kaneko K, Terada K, Kyoya T, Kishino Y. Global–local analysis of granular media in quasi-static equilibrium. Int J Solids Struct 2003;40:4043–69.
[23] Miehe C, Dettmar J, Zäh D. Homogenization and two-scale simulations of granular materials for different microstructural constraints. Int J Numer Methods Eng 2010;83:1206–36.
[24] Nguyen TK, Combe G, Caillerie D, Desrues J. FEM×DEM modelling of cohesive granular materials: numerical homogenisation and multi-scale simulations. Acta Geophys 2014;62(5):1109–26.
[25] Li X, Liang Y, Duan Q, Schrefler B, Du Y. A mixed finite element procedure of gradient Cosserat continuum for second-order computational homogenisation of granular materials. Comput Mech 2014;54:1331–56.
[26] Gross L, Bourgouin L, Hale AJ, Mühlhaus H-B. Interface modeling in incompressible media using level sets in Escript. Phys Earth Planet In 2007;163:23–34.
[27] Šmilauer V, et al. Using and programming. In: Yade documentation, the Yade project, 2nd ed.; 2015. http://dx.doi.org/10.5281/zenodo.34043.
[28] Wren JR, Borja RI. Micromechanics of granular media Part II: Overall tangential moduli and localization model for periodic assemblies of circular disks. Comput Methods Appl Mech Eng 1997;141:221–46.
[29] Kruyt N, Rothenburg L. Statistical theories for the elastic moduli of two-dimensional assemblies of granular materials. Int J Eng Sci 1998;36:1127–42.
[30] Thornton C. Numerical simulations of deviatoric shear deformation of granular media. Géotechnique 2000;50(1):43–53.
[31] Stroeven M, Askes H, Sluys L. Numerical determination of representative volumes for granular materials. Comput Methods Appl Mech Eng 2004;193:3221–38.
[32] Hashin Z. Analysis of composite materials—a survey. J Appl Mech 1983;50:481–505.
[33] Drugan W, Willis J. A micromechanics-based nonlocal constitutive equation and estimates of representative volume element size for elastic composites. J Mech Phys Solids 1996;44:497–524.
[34] Satake M. Fabric tensor in granular materials. In: IUTAM symposium on deformation and failure of granular materials. Delft: A.A. Balkema; 1982. p. 63–8.
[35] Guo N, Zhao J. The signature of shear-induced anisotropy in granular media. Comput Geotech 2013;47:1–15.
[36] Dalcín L, Paz R, Storti M. MPI for Python. J Parall Distrib Comput 2005;65:1108–15.
[37] Dalcín L, Paz R, Storti M, D'Elía J. MPI for Python: performance improvements and MPI-2 extensions. J Parall Distrib Comput 2008;68:655–62.
[38] Geuzaine C, Remacle J-F. Gmsh: a 3-D finite element mesh generator with built-in pre- and post-processing facilities. Int J Numer Methods Eng 2009;79:1309–31.
[39] Marachi ND, Duncan JM, Chan CK, Seed HB. Plane-strain testing of sand. In: Yong RN, Townsend FC, editors. Laboratory shear strength of soil, ASTM STP740. ASTM; 1981. p. 294–302.
[40] Desrues J, Chambon R, Mokni M, Mazerolle F. Void ratio evolution inside shear bands in triaxial sand specimens studied by computed tomography. Géotechnique 1996;46(3):529–46.
[41] Higo Y, Oka F, Kimoto S, Sanagawa T, Matsushima Y. Study of strain localization and microstructural changes in partially saturated sand during triaxial tests using microfocus X-ray CT. Soils Found 2011;51(1):95–111.
[42] Hall SA, Bornert M, Desrues J, Pannier Y, Lenoir N, Viggiani G, et al. Discrete and continuum analysis of localised deformation in sand using X-ray μCT and volumetric digital image correlation. Géotechnique 2010;60(5):315–22.
[43] Bardet JP, Proubet J. A numerical investigation of the structure of persistent shear bands in granular media. Géotechnique 1991;41(4):599–613.
[44] Calvetti F, Combe G, Lanier J. Experimental micromechanical analysis of a 2D granular material: relation between structure evolution and loading path. Mech Cohes-Frict Mater 1997;2:121–63.
[45] Andó E, Hall SA, Viggiani G, Desrues J, Bésuelle P. Grain-scale experimental investigation of localised deformation in sand: a discrete particle tracking approach. Acta Geotech 2012;7(1):1–13.
[46] Zhao J, Guo N. Unique critical state characteristics in granular media considering fabric anisotropy. Géotechnique 2013;63(8):695–704.
[47] Mollon G, Zhao J. Fourier–Voronoi-based generation of realistic samples for discrete modelling of granular materials. Granul Matter 2012;14:621–38.
[48] Mollon G, Zhao J. Generating realistic 3D sand particles using Fourier descriptors. Granul Matter 2013;15:95–108.
[49] Mollon G, Zhao J. 3D generation of realistic granular samples based on random fields theory and Fourier shape descriptors. Comput Methods Appl Mech Eng 2014;279:46–65.